Novel Mechanical Response of Parallelogram-Face Origami Governed by Topological Characteristics

Yanxin Feng,[1] Andrew Wu,[1] James McInerney,[2] Siddhartha Sarkar,[2] Xiaoming Mao,[2] and D. Zeb Rocklin[1]
[1]School of Physics, Georgia Institute of Technology, Atlanta, Georgia 30332, USA
[2]Department of Physics, University of Michigan, Ann Arbor, Michigan 48109, USA

(Received 26 November 2024; accepted 24 September 2025; published 20 November 2025)

Origami principles are used to create strong, lightweight structures with complex mechanical response. However, identifying the fundamental physical principles that determine a sheet's behavior remains a challenge. We introduce a new analytic theory to account for the low-energy, spatially varying deformations of parallelogram-face origami, a broad class that includes widely studied sheets. We identify topological classes—previously predicted in quantum systems—with sharply distinct mechanical properties, offering a mechanism for control over origami's effective stiffness and the smoothness of its mechanical response to external loads. The key control parameter is the Poisson's ratio; when it is negative, as in the Miura ori, sheets have conventional, smooth mechanical response amenable to continuum-based approaches. In contrast, positive Poisson's ratio, as in the eggbox ori, generates a topological transition to lines of doubly degenerate zero modes that lead to dramatically softer structures with uneven, complex patterns of spatial response. These patterns interact in complicated ways with origami boundary conditions and source terms, leading to rich physical phenomena in experimentally accessible systems. Indeed, these rich topological phenomena demonstrate that the complex response of some origami sheets is both intrinsic and topological in origin and cannot be captured via continuum-based approaches. Doubly degenerate modes, such as the topological ones identified here, are related to non-Abelian physics and coherent computing paradigms. By exploring such consequences and extending the theory to the broader class of origami with nonparallelogram faces, this work sheds light on intriguing new areas of physics.

DOI: 10.1103/gdb2-grvp

Subject Areas: Metamaterials, Soft Matter

I. INTRODUCTION

Origami sheets are two-dimensional structures constructed by generating patterns of creases along which they can fold at a low energy cost. Originally developed only for their recreational and aesthetic values, these sheets have intrigued mathematicians [1], computer scientists [2,3], and physicists [4,5], as well as engineers who seek novel metamaterials [6,7] or want to design robots [8–10]. The geometry of origami sheets, as defined by their crease patterns, can result in dramatically different responses when external loads are applied. The large space of possible crease patterns allows origami sheets to exhibit exotic mechanical properties beyond those of the original sheets of paper—such as a tunable Poisson's ratio [11], multidirectional auxeticity [12], programmability [13], and deployability [14]—making origami-inspired structures widely applicable in different fields.

Despite these broad applications, it is challenging to predict and control the nonuniform deformations of origami sheets under general loading [15]. To address this issue, we take an approach that first became prevalent in analyzing quantum mechanical systems and later was applied to analogous classical mechanical systems—the topological classification. In quantum mechanics, since the discovery of special quantum states [16] that are topologically distinct and lead to quantization associated with certain topological invariants [17], physicists have been engaged in looking for systems with novel topological signatures, as well as classifying them accordingly. The most well-known classification, the tenfold way, was established by Altland and Zirnbauer [18,19], and there are other variants based on this type, such as the threefold way introduced for non-Hermitian matrices [20]. This approach allows physicists to better understand phenomena like the quantum Hall effect and to infer important properties such as the band structure in different quantum systems, including topological insulators [21]. In classical mechanical systems, researchers strive to explore novel mechanical properties indicated by similar topological invariants. For instance, the quantum Su-Schrieffer-Heeger (SSH) model [22] has a classical mechanical

Published by the American Physical Society under the terms of the Creative Commons Attribution 4.0 International license. Further distribution of this work must maintain attribution to the author(s) and the published article's title, journal citation, and DOI.

counterpart introduced by Kane and Lubensky via a 1D isostatic lattice [23]. "Topological insulators" were realized in various mechanical systems as well [24–26]. These works show how edge states are controlled by the topological invariants in the bulk (the bulk-boundary correspondence) and how a topological approach is necessary to understand the behavior of such systems. In the field of origami, topology can also play a vital role in determining zero-energy deformations [4] or localized deformation [27], and it can provide new insights into the analysis of its mechanical properties [28,29]. However, generic 2D periodic origami sheets are shown to have no topological polarization [27].

In this paper, we examine a particular class of origami, one with parallelogram faces, with a focus on the Morph patterns [30]. We extend the vertex-amplitude formalism developed in Ref. [5] to nonuniform Bloch modes, developing a band theory that preserves the symmetry of the underlying origami faces. We find that these symmetries lead to a novel topological invariant given by the Pfaffian [31]. This topological invariant also underlies the quantum spin Hall effect [32] and has previously been applied to a continuum mechanical system [33]. We find that auxetic origami, such as the Miura [34,35], is topologically trivial, but nonauxetic origami, such as the eggbox [36,37], has a nontrivial invariant that leads to lines of doubly degenerate zero modes stretching across the Brillouin zone, strongly modifying the origami's mechanical response with modes activated at finite wavelength. This finding sheds new light on the challenge of achieving targeted deformations of these broad classes of origami sheets, as well as providing insight into how to characterize and control them via reciprocal-space methods.

This paper is organized as follows. In Sec. II, we introduce our system and characterize its topological properties using a novel formalism based on the origami sheet's symmetries. In Sec. III, we consider how interplay between origami stretching and bending informs the response of the system. In Sec. IV, we simulate origami sheets from distinct topological classes and characterize their sharply distinct responses. In Sec. V, we discuss the implications of our work.

II. SIGN OF PFAFFIAN AS TOPOLOGICAL CHARGE GOVERNS MECHANICAL RESPONSE

A. Geometry of parallelogram-based origami and description of deformation via folding amplitudes

We consider origami sheets consisting of repeating unit cells indexed by $\mathbf{n} = (n_1, n_2)$, each of which contains four parallelogram faces, as in Ref. [5]. The geometry of these faces is set by their edge lengths and sector angles as in Fig. 1(a). Once the geometry of the faces is fixed, the spatial embedding of the sheet is determined by the dihedral angles of adjoining faces. We restrict ourselves to systems with a common edge length and at most two parallelogram geometries set by their sector angles α, β, which is the class of Morph origami [30]. As special cases, we also consider $\beta = \alpha$, the eggbox crease pattern [38,39], and $\beta = \pi - \alpha$, the Miura fold [34,40]. Examples of such origami sheets as well as their unit cells are shown in Fig. 1. This range of systems suffices to realize the range of topological classes and types of mechanical response on which we focus. Each vertex of one of these parallelogram-based origami sheets possesses a 1D family of nonlinear isometries, foldings of the adjoining edges that do not stretch the adjoining faces [41]. The geometry of different vertices is compatible so that each sheet possesses a rigid, uniform folding motion, as shown in Fig. 1(b). For origami sheets made out of conventional materials such as paperboard or metal, the energy cost of stretching the faces of the sheets is much higher than that of bending or folding the sheets. Hence, those isometries are low-energy modes favored by origami sheets, and in the ideal case where we neglect the energy associated with folding and bending, they become the zero-energy modes. We thus refer to these isometries as "zero modes" despite the inclusion in our numerical modeling of weak bending stiffness that converts the actual physical response to low-energy "soft modes." Where previously only uniform deformations were considered [5], we now consider a linearized but nonuniform version of these modes, in which the degree to which a vertex is folded along this manifold of isometries is given by its folding amplitude $\mathcal{V}$. In a unit cell, there are four vertices, labeled a, b, c, d as shown in Fig. 1(a). We may refer to a potential isometric deformation of the sheet by a set of folding amplitudes at each vertex in each cell, denoted $\mathcal{V}^a(\mathbf{n})$. Folding two vertices with a shared edge by different amounts implies that the dihedral angle varies along the length of the edge [5], and therefore, the adjoining faces are bending (a nonrigid isometry). Conditions for compatible face bending are derived in the Supplemental Material [42]. This formalism applies quite generally to origami sheets with parallelogram faces. It may be possible to extend the formalism to spatially varying origami sheets with more general quadrilateral faces, as has recently been done for the uniform case [43].

We are particularly interested in z-periodic modes [4,44], those of the form

$$\mathcal{V}^a(\mathbf{n}) \equiv \mathcal{V}^a(\mathbf{0})\mathbf{z}^{\mathbf{n}} \equiv \mathcal{V}^a z_1^{n_1} z_2^{n_2}, \tag{1}$$

which extends Bloch's theorem [45] by allowing the wave vectors to not be purely real so as to permit edge modes localized at the boundaries of finite sheets. Bulk modes are the special case of $\mathbf{z} = e^{i\mathbf{q}}$, with $\mathbf{q}$ a purely real wave vector in the Brillouin zone.

The aforementioned (linearized) global isometries correspond to modes $z_1 = z_2 = 1$. For a nonuniform global isometry, the compatibility conditions on the folding

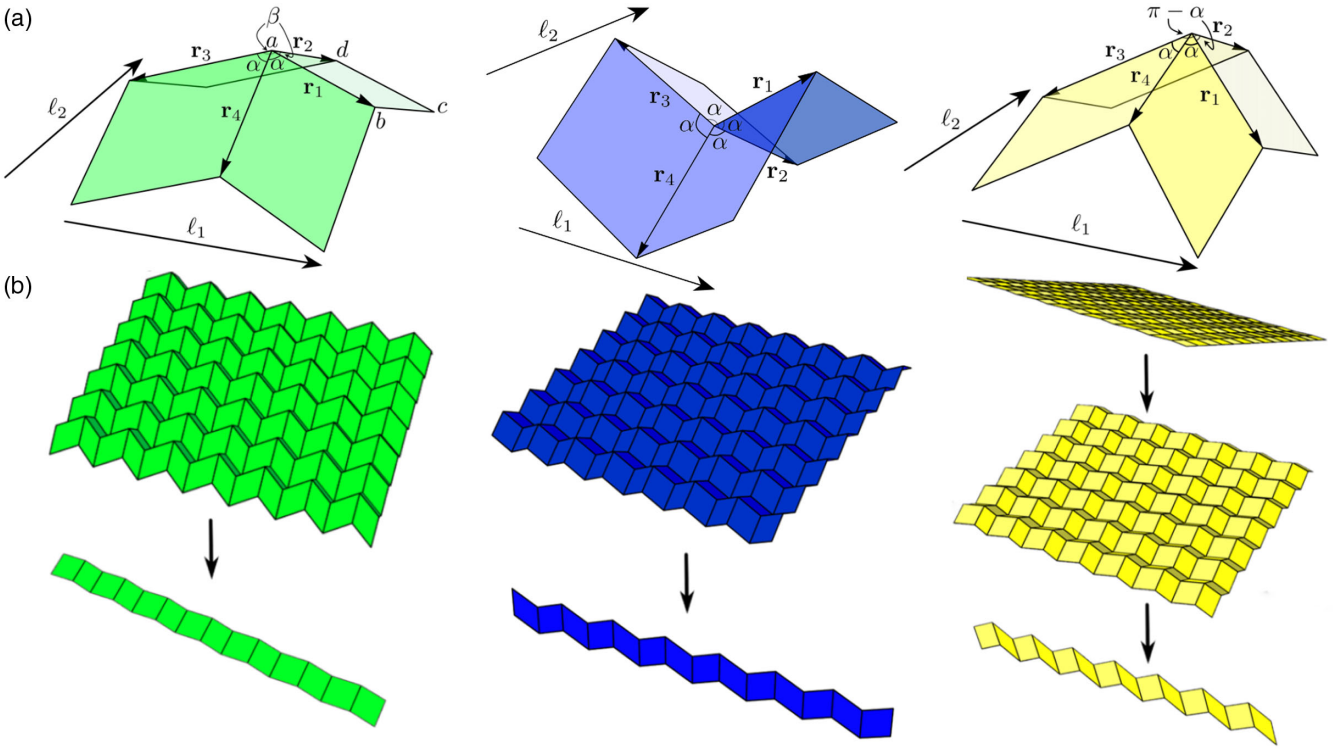


FIG. 1. (a) Geometry of an origami unit cell of the Morph structure, consisting of four parallelogram faces with sector angles $\alpha, \alpha, \beta, \beta$ at a single vertex. Here, $\mathbf{r}_i$ are edge vectors around the vertex a, and ℓ_1, ℓ_2 are the two lattice vectors. The generic case (green, left) is known as the Morph, the symmetric case (blue, center) is known as the eggbox and has four equal angles α, and the developable case (yellow, right) is known as the Miura and has $\beta = \pi - \alpha$. (b) Folding mechanisms of the different types of origami. A generic Morph pattern is always flat-foldable (meaning that it can be rigidly folded into a flat state), but only the Miura (the yellow one) is developable, meaning that it corresponds to a crease pattern applied to a flat sheet of paper.

amplitudes between neighboring vertices impose linear, homogeneous constraints among local isometries $\mathcal{V}^a(\mathbf{n})$ across different cells. In the Supplemental Material [42], we explicitly show how the constraint on each vertex in the unit cell can be represented as a corresponding row in a 4×4 matrix, which we denote as the folding compatibility matrix. The constraint equations are then written as

$$\mathbf{C}(\mathbf{z})|\mathcal{V}\rangle = \mathbf{0}, \tag{2}$$

where $|\mathcal{V}\rangle = (\mathcal{V}^a, \mathcal{V}^b, \mathcal{V}^c, \mathcal{V}^d)^T$ is the vector representing folding amplitudes of four vertices in a unit cell, and

$$\mathbf{C}(\mathbf{z}) = \begin{pmatrix} X_1 + X_2 - X_3 - X_4 & -X_1 + z_1^{-1}X_3 & 0 & -X_2 + z_2^{-1}X_4 \\ -X_1 + z_1 X_3 & X_1 - X_2 - X_3 + X_4 & X_2 - z_2^{-1}X_4 & 0 \\ 0 & X_2 - z_2 X_4 & -X_1 - X_2 + X_3 + X_4 & X_1 - z_1 X_3 \\ -X_2 + z_2 X_4 & 0 & X_1 - z_1^{-1}X_3 & -X_1 + X_2 + X_3 - X_4 \end{pmatrix}. \tag{3}$$

The X_i's in Eq. (3) are folding coefficients given by

$$X_i = \hat{\mathbf{r}}_{i+1} \cdot (\hat{\mathbf{r}}_{i+2} \times \hat{\mathbf{r}}_{i+3})/r_i, \tag{4}$$

where the $\mathbf{r}_i$'s are edge vectors emanating out counterclockwise from vertex a, defined as in Fig. 1(a). The subscript labels them in a counterclockwise order and is defined modulo 4 since there are 4 edges around each vertex. We emphasize that Eq. (3) is obtained in a uniform reference state, while in a generic case where vertices with the same label across different unit cells are not in the same state, those coefficients are no longer defined globally and should depend explicitly on the cell index as well.

B. Symmetries and topological class

The $\mathbf{C}(\mathbf{z})$ defined in Eq. (3) is a generalized Hermitian in the sense that

$$\mathbf{C}(\mathbf{z})^T = \mathbf{C}(\mathbf{1}/\mathbf{z}), \tag{5}$$

with T denoting the matrix transpose. This result reduces to the well-known Hermitian property $\mathbf{C}(\mathbf{z})^T = \mathbf{C}(\bar{\mathbf{z}}) = \overline{\mathbf{C}(\mathbf{z})}$ inside the Brillouin zone, where $1/\mathbf{z} = \bar{\mathbf{z}}$, with the overbar denoting complex conjugation. Hence, this matrix that describes the allowed linear isometries of an origami sheet can be treated as a Hamiltonian describing the quantum dynamics of a periodic (crystalline) system. For our purpose, because of a spatial inversion symmetry in the parallelogram-based origami system, we adopt the topological classification for centrosymmetric systems introduced in Ref. [46].

We now explicitly consider the symmetries of this Hamiltonian. If we permute the opposite vertices in each parallelogram face, we exchange the mountains and valleys of the crease pattern, producing a global minus sign for $\mathbf{C}(\mathbf{z})$. In addition, since the directions of the two lattice vectors are flipped, the generalized wave vector $\mathbf{z}$ becomes $1/\mathbf{z}$. In the end, we obtain a spatial inversion symmetry in the parallelogram-based origami lattice

$$\mathbf{P}\mathbf{C}(\mathbf{z})\mathbf{P}^{-1} = -\mathbf{C}(1/\mathbf{z}), \tag{6}$$

where the permutation (or inversion) operator $\mathbf{P}$ has the form

$$\mathbf{P} = \begin{pmatrix} 0 & 0 & 1 & 0 \\ 0 & 0 & 0 & 1 \\ 1 & 0 & 0 & 0 \\ 0 & 1 & 0 & 0 \end{pmatrix}. \tag{7}$$

Obviously, we have $\mathbf{P}^2 = \mathbb{I}$. Inspired by classification of quantum operators, we now introduce the complex conjugation operator $\mathbf{K}$, which is antiunitary and maps a complex quantity to its complex conjugate. It serves as the time-reversal symmetry (within the Brillouin zone)

$$\mathbf{K}\mathbf{C}(\mathbf{z})\mathbf{K}^{-1} = \mathbf{C}(1/\mathbf{z}). \tag{8}$$

Composing it with the inversion operator $\mathbf{P}$, we obtain an antiunitary operator [47] $\mathbf{K}\mathbf{P}$ that obeys $(\mathbf{K}\mathbf{P})^2 = \mathbf{K}^2\mathbf{P}^2 = \mathbb{I}$ since $\mathbf{P}$ is purely real and therefore commutes with $\mathbf{K}$, which also squares to the identity. Inside the Brillouin zone, we have

$$(\mathbf{K}\mathbf{P})\mathbf{C}(\mathbf{z})(\mathbf{K}\mathbf{P})^{-1} = \mathbf{K}(\mathbf{P}\mathbf{C}(\mathbf{z})\mathbf{P})\mathbf{K} = -\mathbf{K}\mathbf{C}(\bar{\mathbf{z}})\mathbf{K} = -\mathbf{C}(\mathbf{z}), \tag{9}$$

which corresponds to the particle-hole symmetry introduced in the AZ + $\mathcal{I}$ classification of centrosymmetric systems [46]. Notice that Eq. (9) is local in $\mathbf{z}$, distinct from the standard AZ particle-hole symmetry, in which $\mathbf{z}$ flips to $1/\mathbf{z}$ (in the Brillouin zone, it should flip the wave vector $\mathbf{q}$ to $-\mathbf{q}$). This locality is essential to define a 0D topological invariant, specifically the sign of a Pfaffian, in our 2D Brillouin zone. We show explicitly how to construct this invariant later in this section in Eqs. (17)–(19), but first, we show the existence of a chiral symmetry in our system; hence, our system can be categorized into the BDI class [46].

Take $\theta(z_1) \equiv \arg(X_1 - X_3 z_1)$ and construct a unitary matrix as below, which acts as a mirror symmetry in the reciprocal space,

$$\mathbf{M}_1(z_1) \equiv \begin{pmatrix} e^{i\theta} & & & \\ & e^{-i\theta} & & \\ & & e^{-i\theta} & \\ & & & e^{i\theta} \end{pmatrix}, \tag{10}$$

with the property

$$\mathbf{M}_1(z_1)\mathbf{C}(z_1, z_2)\mathbf{M}_1(z_1)^{-1} = \mathbf{C}(\overline{z_1}, z_2). \tag{11}$$

Similarly, if we take $\phi(z_2) \equiv \arg(X_2 - X_4 z_2)$, we have another unitary matrix

$$\mathbf{M}_2(z_2) \equiv \begin{pmatrix} e^{i\phi} & & & \\ & e^{i\phi} & & \\ & & e^{-i\phi} & \\ & & & e^{-i\phi} \end{pmatrix}, \tag{12}$$

which satisfies

$$\mathbf{M}_2(z_2)\mathbf{C}(z_1, z_2)\mathbf{M}_2(z_2)^{-1} = \mathbf{C}(z_1, \overline{z_2}). \tag{13}$$

The composition of three unitary operators $\mathbf{P}\mathbf{M}_1\mathbf{M}_2$ is still unitary (where we suppress the arguments $z_{1,2}$ in $\mathbf{M}_{1,2}$ for now); a direct calculation shows that it squares to the identity

$$(\mathbf{P}\mathbf{M}_1\mathbf{M}_2)^2 = \mathbb{I}, \tag{14}$$

and its action on the $\mathbf{C}(\mathbf{z})$ is given by

$$(\mathbf{P}\mathbf{M}_1\mathbf{M}_2)\mathbf{C}(\mathbf{z})(\mathbf{P}\mathbf{M}_1\mathbf{M}_2)^{-1} = \mathbf{P}\mathbf{C}(\bar{\mathbf{z}})\mathbf{P}^{-1} = -\mathbf{C}(\mathbf{z}), \tag{15}$$

which is exactly the chiral symmetry.

With all three symmetries Eqs. (8), (9), and (15) and the positive signatures, our system is categorized into the BDI classes of both the AZ and AZ + $\mathcal{I}$ schemes [46], the latter of which ensures the sign of a Pfaffian as its 0D topological charge. For an antisymmetric $2n \times 2n$ matrix $A = (a_{ij})$, the Pfaffian is defined to be

$$\mathrm{Pf}\, A = \frac{1}{2^n n!} \sum_{\sigma \in S_{2n}} \mathrm{sgn}(\sigma) \prod_{i=1}^{n} a_{\sigma(2i-1),\sigma(2i)}, \tag{16}$$

where S_{2n} is the symmetric group of order $(2n)!$ and $\mathrm{sgn}(\sigma)$ is the signature of the permutation σ. Note that our $\mathbf{C}(\mathbf{z})$ is not antisymmetric, even when $\mathbf{z}$ is inside the Brillouin zone. To resolve this apparent discrepancy, we can perform a change of basis and render $\mathbf{C}(\mathbf{z})$ into an antisymmetric form. To reach this goal, consider

$$\mathbf{U} \equiv \mathbf{P}^{1/2} = \frac{1}{2}(\mathbb{I} + \mathbf{P}) + \frac{i}{2}(\mathbb{I} - \mathbf{P}), \tag{17}$$

which is unitary. We then perform a unitary transformation $\tilde{\mathbf{C}}(\mathbf{z}) \equiv \mathbf{U}\mathbf{C}(\mathbf{z})\mathbf{U}^{-1}$, and it follows from direct calculation that Eq. (6) becomes

$$\tilde{\mathbf{C}}(\mathbf{z}) = -\tilde{\mathbf{C}}^T(\mathbf{z}), \tag{18}$$

which shows that $\tilde{\mathbf{C}}(\mathbf{z})$ is now antisymmetric and hence the definition of Pfaffian is justified. We denote by $\{\tilde{c}_{ij}\}_{i,j=1}^{4}$ the entries of $\tilde{\mathbf{C}}(\mathbf{z})$. These entries clearly depend on $\mathbf{z}$, but here we omit it for convenience. We have

$$\begin{aligned}\mathrm{Pf}\, \tilde{\mathbf{C}}(\mathbf{z}) &= \tilde{c}_{12}\tilde{c}_{34} - \tilde{c}_{13}\tilde{c}_{24} + \tilde{c}_{14}\tilde{c}_{23} \\ &= X_1 X_3 (z_1 - 1)^2/z_1 - X_2 X_4 (z_2 - 1)^2/z_2,\end{aligned} \tag{19}$$

which is true for a general complex wave vector $\mathbf{z}$ not necessarily inside the Brillouin zone. According to the property of a Pfaffian that its square is equal to the determinant, we have

$$(\mathrm{Pf}\, \tilde{\mathbf{C}}(\mathbf{z}))^2 = \det \tilde{\mathbf{C}}(\mathbf{z}) = \det \mathbf{C}(\mathbf{z}). \tag{20}$$

Notice that because of the chiral symmetry in Eq. (15), the eigenvalues of $\mathbf{C}(\mathbf{z})$ are always paired $\pm\lambda$; thus, $\det \mathbf{C}(\mathbf{z})$, which is equal to the product of all its eigenvalues, is non-negative. Hence, the Pfaffian on the left-hand side of Eq. (20) is purely real inside the Brillouin zone. In the next section, we consider the implications for mechanical response for two topological classes: those sheets in which the sign of the Pfaffian is uniform across the Brillouin zone and those sheets in which it changes.

C. Topological classes determined by geometric factors and lattice Poisson's ratio

Depending on whether the Pfaffian changes its sign in the Brillouin zone, parallelogram-based origami sheets can be categorized into two distinct classes: conventional and topological. The conventional sheets are those with a uniform sign of the Pfaffian inside the Brillouin zone, except for the origin where the determinant always vanishes. The topological sheets are those for which the Pfaffian changes signs between two regions in the Brillouin zone separated by a topologically protected one-dimensional line as shown in Fig. 2. Because the Pfaffian is the square root of the determinant, the determinant has a double root along this line, indicating doubly degenerate pairs of topologically protected zero modes.

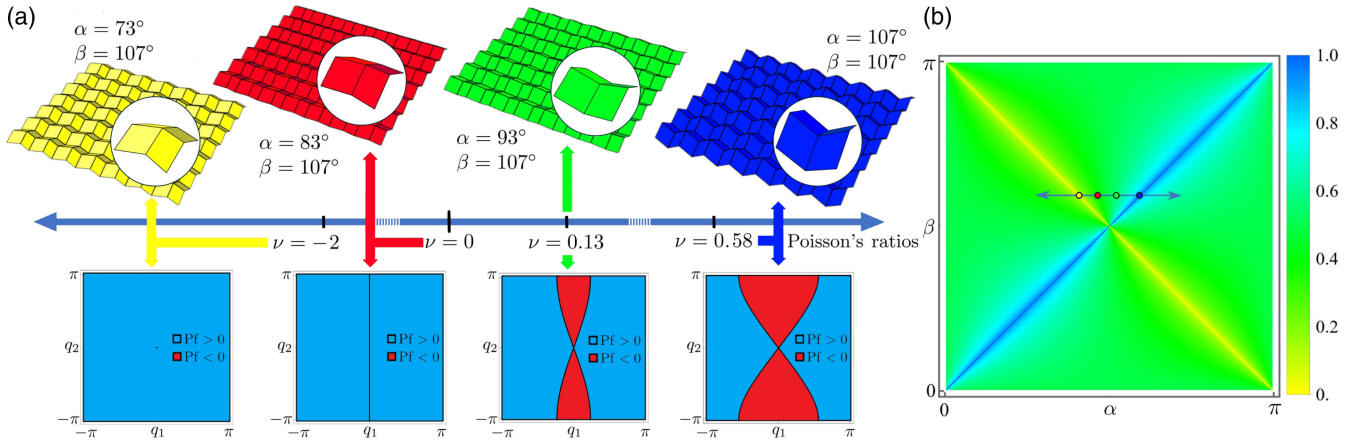


FIG. 2. (a) Morph patterns (top) with only slightly different folding modes, which have rigid folding with significantly different Poisson ratios ν. For auxetic systems ($\nu < 0$), the topological invariant (sign of the Pfaffian) described in the main text has the same sign across the entire Brillouin zone (bottom), and the only bulk zero modes are at the origin, indicating long-wavelength behavior. For anauxetic systems ($\nu > 0$), the invariant changes sign within the Brillouin zone, indicating doubly degenerate lines of zero modes (black), such that a low-energy response can occur at short wavelengths. The transition between the two cases occurs at ($\nu = 0$) with a vertical line of zero modes. (b) Nonlinear folding mode for each origami sheet, as shown in Fig. 1. This mode changes the Poisson's ratio and hence the presence of topological modes. The plot shows the fraction of configurations for a given sheet that have topological modes, ranging from 0 (Miura) to 1 (eggbox). The blue arrow indicates our transition in part (a) from the Miura (left) to the eggbox (right), with four points corresponding to the four sheets with same colors in part (a).

Inside the Brillouin zone, Eq. (19) becomes

$$\mathrm{Pf}\,\tilde{\mathbf{C}}(\mathbf{q}) = 4\left(X_1X_3\sin^2\left(\frac{q_1}{2}\right) - X_2X_4\sin^2\left(\frac{q_2}{2}\right)\right). \quad (21)$$

As shown in Ref. [5], the lattice Poisson's ratio (the negative ratio of strains in the two lattice directions when the folding mode is activated) is

$$\nu = \frac{|l_2|^2}{|l_1|^2}\frac{X_2X_4}{X_1X_3}. \quad (22)$$

From these two expressions, it immediately follows that the existence of lines of zero modes in the Brillouin zone is completely determined by the sign of the Poisson's ratio. The Poisson's ratio of a Miura-ori shown in Fig. 1 is well known to always be negative. Hence, the Pfaffian never flips its sign in the Brillouin zone, and the only bulk zero mode occurs trivially at the origin with $q_1 = q_2 = 0$.

In contrast to the Miura, the eggbox sheet in Fig. 2 always has a positive Poisson's ratio and thus always has doubly degenerate lines of zero modes. The eggbox family thus fits into the category of topological lattices. For a generic Morph pattern, since its Poisson's ratio can take both positive and negative values [30], its topological class depends not only on the unit cell geometry but also on the particular spatial embedding. Using the Morph family, we are able to transit from a purely conventional lattice (a Miura) to a purely topological one (an eggbox) as in Fig. 2. Notably, the positive Poisson ratio that admits a topologically nontrivial response arises only for nondevelopable sheets. While this might not be true universally, developed sheets must have a negative Poisson ratio in the flat configuration since they cannot expand in either direction.

Four sample lattices—one from the Miura, two from the Morph, and one from the eggbox family—are shown in Fig. 2 to demonstrate a topological transition. As ν varies along the axis, lines of zero modes emerge vertically in the Brillouin zone at $\nu = 0$ and, for a generic $\nu > 0$, form an "X" shape that gradually flattens and finally merges into a single horizontal line of zero modes $q_2 = 0$ at $\nu = +\infty$.

In the next section, we illustrate in detail how the topological transition fundamentally changes the mechanical response of the sheet under external loads.

III. THEORETICAL ANALYSIS OF MECHANICAL RESPONSE

A. Description of deformation via vertex displacements and change of dihedral angles

To investigate how these topological modes determine the response of an origami sheet to an external load, we adopt another formalism to describe deformation. In previous sections, we use the 4×4 compatibility matrix in Eq. (3) to ensure geometric compatibility between neighboring vertices. This approach has the advantage of simplifying the description of isometric deformations to the point that the fundamental symmetries that govern the topological class can be discerned. However, such formulations cannot capture generic loading conditions in which panels are stretched as well as bent. To address this issue, we now describe a deformation of the $\mathbf{n}$th unit cell by a 12D vector $\mathbf{u}(\mathbf{n})$. This vector is obtained by concatenating four 3D vectors, each representing the displacement of one of the cell's vertices [44]. Again, we assume a z periodicity for the displacement vector:

$$\mathbf{u_z}(\mathbf{n}) \equiv \mathbf{u_z}(n_1, n_2) \equiv z_1^{n_1} z_2^{n_2}\mathbf{u_z}(\mathbf{0}) \equiv \mathbf{z^n u_z}. \quad (23)$$

In the case of an isometric deformation, it is possible to convert between vertex displacements and vertex folding, up to a uniform translation of the whole sheet, which does not induce any folding. Generic deformations to the origami sheet cost energy, which we can model by placing springlike elements along the edges of origami panels. Because bending costs energy but does not stretch any edge, we also add a spring along a diagonal of each quadrilateral panel. One might be concerned with which diagonal to add, but the Supplemental Material [42] shows qualitatively the same (but not exactly the same) results for the two choices of diagonal. Therefore, it is a somewhat arbitrary choice to make, at least within the scope of the discussion in this paper, since all the important results discussed here—the existence of topological modes, the impact on stiffness, and jaggedness of response—are unaffected. To see the effect of infinitesimal displacements on those virtual springs, we introduce the rigidity matrix $\mathbf{R}(\mathbf{z})$ [48]. The literature also refers to this matrix as the compatibility matrix, but we prefer calling it the rigidity matrix in this paper, in order to avoid confusion with the $\mathbf{C}(\mathbf{z})$ matrix already defined in Eq. (3). The rigidity matrix $\mathbf{R}(\mathbf{z})$ relates the infinitesimal z-periodic displacements $\mathbf{u_z}$ to resulting z-periodic extensions $\mathbf{e_z}$ in bars (a compression being a negative extension) via

$$\mathbf{e_z} = \mathbf{R}(\mathbf{z})\mathbf{u_z}, \quad (24)$$

and the dependence of $\mathbf{R}(\mathbf{z})$ on $\mathbf{z}$ is due to the existence of intercellular bars. Zero modes are, by definition, the null vectors of $\mathbf{R}(\mathbf{z})$ such that $\mathbf{R}(\mathbf{z})\mathbf{u_z} = \mathbf{0}$, which also coincide with isometries.

We comment further on the relation between the compatibility matrix $\mathbf{C}$ and the rigidity matrix $\mathbf{R}$ to illustrate why we need the two types of formalisms. They are equivalent in describing the isometric deformation (zero modes), respectively, by describing how the sheet folds around each vertex (for the compatibility matrix) and how each vertex is displaced in the 3D space (for the rigidity matrix), except for the trivial isometries like global translations and rotations. They are different in the sense that the

compatibility matrix only describes isometric modes, and it cannot determine the response of the sheet under a generic external load, which may induce a nonisometric deformation. However, for the rigidity matrix, it gives the resultant extension (or compression) of edges when the vertices are displaced, and one can infer the dynamics of the system once the constitutive law of the edges is specified (for instance, we treat them as simple Hookean springs in this work). The rigidity matrix can be defined for any generic spring-mass system, even for a non-Maxwell lattice where the number of constraints is not equal to the number of degrees of freedom; however, in this case, it will not be a square matrix, and it lacks the essential symmetries to easily define a topological invariant. Therefore, we need to employ both formalisms—the compatibility matrix to exploit the symmetry of the sheets and to define the topological invariant, and the rigidity matrix to infer mechanical responses of the sheets under generic external loads.

There are 12 bars in each unit cell, so $\mathbf{e_z}$ is also 12D and $\mathbf{R}(\mathbf{z})$ is a 12×12 square matrix. Thus, our system is at the mechanical critical point where the number of degrees of freedom is equal to the number of constraints. For such systems, the Maxwell-Calladine index theorem [44,49,50] ensures that a zero mode at $\mathbf{z}$ implies a state of self-stress (a force-balanced configuration in which tensions in bars joining at the same vertex result in a zero net force on the vertex) at $1/\mathbf{z}$. When $\mathbf{z}$ is complex, indicating exponential growth, the two modes are exponentially localized at opposite edges. In the special case of bulk modes ($\mathbf{z}$ real), one bulk zero mode at a certain wave vector corresponds to a state of self-stress at its opposite wave vector. For any triangulated origami sheets (not necessarily parallelogram-based), apart from this correspondence at opposite wave vectors, there is another hidden symmetry [4] that establishes a duality between zero modes and states of self-stress at the same wave vector $\mathbf{z}$. Combining the hidden symmetry with the index theorem, we know that a zero mode at $\mathbf{z}$ give rises to another zero mode at $1/\mathbf{z}$. Therefore, zero modes appear in pairs on different edges, meaning that they are never polarized on one edge [20,27], revealing that all two-dimensional sheets are topologically trivial within the Kane-Lubensky scheme of classifying topological mechanical modes [23].

The determinant of $\mathbf{R}(\mathbf{z})$, when expanded into a Laurent polynomial in a proper gauge, has a palindromic form

$$\det \mathbf{R}(\mathbf{z}) = \sum_{m,n} c_{mn} z_1^m z_2^n, \tag{25}$$

with $c_{mn} = c_{-m,-n}$. Here, a gauge change means an overall division of $z_1^i z_2^j$ with some integers i, j to make the coefficients match up. In particular, inside the Brillouin zone where $|z_1| = |z_2| = 1$, zero modes appear in pairs at opposite real wave vectors. Furthermore, taking complex conjugates of both sides in Eq. (25) and using the palindromic property $c_{mn} = c_{-m,-n}$, we see that $\det \mathbf{R}(\mathbf{z}) = \overline{\det \mathbf{R}(\mathbf{z})}$, which forces the determinant of $\mathbf{R}(\mathbf{z})$ to be real inside the 2D Brillouin zone.

Notice that, even though Eq. (21) is already shown to be real inside the Brillouin zone, the realness of Eq. (25) does not require the origami to be parallelogram-based at all. Thus, we can extend the topological classification of origami to any general triangulated periodic lattice by considering whether the sign of $\det \mathbf{R}(\mathbf{z})$ is conserved inside the Brillouin zone, and the conclusions we draw in this and the following sections carry over to the case of generic triangulated lattices as well.

In order to take into account energy associated with folding along creases and bending of faces, which lifts the topological zero modes and turns them into soft modes, we introduce another 12D vector $\boldsymbol{\phi}$, representing the change of dihedral angles along creases. We treat the effect of bending a parallelogram face the same as folding along its diagonal crease, even though crease folding and face bending are quantitatively different in practice. There are two main reasons to justify this simplification. One is that the topological signature of our system depends only on the rigidity matrix $\mathbf{R}(\mathbf{z})$, which reflects the behavior of the bars and does not distinguish crease folding from face bending. The second reason is that, for real paperboard origami sheets, the energy costs of accommodating an external load via bending a face or folding along a crease are comparable, whereas stretching a face would require several orders of magnitude more energy [36,51].

The $\boldsymbol{\phi}$ induced by a z-periodic displacement is also z periodic, and we attach a $\mathbf{z}$ subscript to emphasize this dependence. By constructing an angular velocity field over the sheet as in Refs. [4,5], we can find an explicit linear map $\mathbf{S}(\mathbf{z})$ [48] that sends $\mathbf{u_z}$ to $\boldsymbol{\phi}_\mathbf{z}$,

$$\boldsymbol{\phi}_\mathbf{z} = \mathbf{S}(\mathbf{z})\mathbf{u_z}. \tag{26}$$

This matrix also has the dimension 12×12 since each dihedral angle corresponds to a bar when there is no open boundary. The construction of this matrix is demonstrated in the Supplemental Material [42].

B. Quadratic energy functional and mechanical response

In this section, we deduce a scaling law for the dominant response for topological sheets near soft modes under periodic boundary conditions in Eq. (23). From the dominant part, we can further predict that the effective stiffness of topological sheets should obey certain power laws, which are also verified numerically.

As the vertices displace, energy is required for the origami sheet to stretch and fold. In particular, under periodic boundary conditions, we may assume the displacements to be modulated by a Bloch phase factor $e^{i\mathbf{q}}$, which is

a special case of Eq. (23) with z_1, z_2 in the Brillouin zone. Correspondingly, the rigidity matrix $\mathbf{R}(e^{i\mathbf{q}})$ depends on the wave vector $\mathbf{q}$ [52], and, for simplicity in notation, we denote it by $\mathbf{R}(\mathbf{q})$ from now on. The same change of notation applies to $\mathbf{S}$ as well. Under an external load, we introduce the quadratic energy functional E_{tot} to our system, induced by the periodic displacements $\mathbf{u_q}$,

$$E_{\text{tot}} = \sum_{\mathbf{q}} \frac{1}{2}\mathbf{u}_{-\mathbf{q}}^T \mathbf{S}^T(-\mathbf{q})\mathbf{K_f}\mathbf{S}(\mathbf{q})\mathbf{u_q} + \frac{1}{2}\mathbf{u}_{-\mathbf{q}}^T \mathbf{R}^T(-\mathbf{q})\mathbf{K_s}\mathbf{R}(\mathbf{q})\mathbf{u_q}, \tag{27}$$

where $\mathbf{K_s}$ is a diagonal matrix whose elements represent force constants of the bars and, likewise, $\mathbf{K_f}$ is that of rotational springs associated with folding along creases. The exact values of elements in these two matrices, in general, depend on the particular geometry of the origami sheet as well as its specific embedding, but their orders of magnitude are uniform across a homogeneous sheet made up of the same material. Therefore, for convenience in discussion, we denote by k_s and k_f, respectively, the representative orders of magnitude of diagonal elements in $\mathbf{K_s}$ and $\mathbf{K_f}$. For paperboard origami sheets, the numerical values are approximately $k_s = 10^6$ $(\text{N}\cdot\text{m}^{-1})$ and $k_f = 0.1$ $(\text{N}\cdot\text{m})$ [36,51]. For an origami sheet with average panel area $A \gtrapprox 10^{-4}$ m^2, we may assume the unitless quantity $k_s A/k_f \gg 1$.

The gradient of this energy function is related to the Fourier-transformed external force $\mathbf{f_q}$ by

$$\mathbf{f_q} = \nabla_{\mathbf{u_q}} E_{\text{tot}} = \mathbf{S}^T(-\mathbf{q})\mathbf{K_f}\mathbf{S}(\mathbf{q})\mathbf{u_q} + \mathbf{R}^T(-\mathbf{q})\mathbf{K_s}\mathbf{R}(\mathbf{q})\mathbf{u_q} \equiv \mathbf{D}(\mathbf{q})\mathbf{u_q}, \tag{28}$$

where we introduce the dynamical matrix $\mathbf{D}(\mathbf{q})$ relating the external load force to the resulting displacement via $\mathbf{f_q} = \mathbf{D}(\mathbf{q})\mathbf{u_q}$. Near the point Z in Fig. 3, with the mass of the vertices taken to be 1, the frequencies of two acoustic modes follow,

$$\omega^2(\mathbf{q}) \approx O(1)(k_f/A) + O(1)k_s|\mathbf{q} - \mathbf{q}_Z|^2, \tag{29}$$

where $\mathbf{q}_Z$ is point Z in the Brillouin zone.

Solving Eq. (28) to determine the response of an origami sheet to a load force involves inverting a 12×12 matrix $\mathbf{D}$ at each wave vector, which is unlikely to prove conceptually insightful. Now, the topological nature of the lattice provides qualitative insight into its mechanical response. In particular, one might assume the bending term in Eq. (28) can be dropped as it is almost negligible given $k_s A/k_f \gg 1$. However, this assumption breaks down if the sheet is topological so that it has lines of soft modes where the stretching energy vanishes and the bending energy plays an important role. Therefore, the two terms are both small and comparable to each other in the case where $\mathbf{q}$ stays very close to the lines of soft modes.

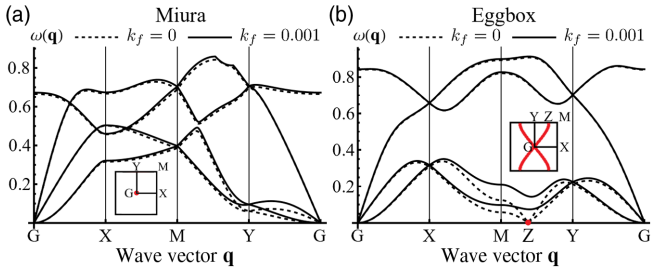


FIG. 3. (a) Dispersion relations of a conventional sheet in the Miura family. The stretching stiffness k_s is set to 1 for simplicity. Dashed lines are for the case of no folding stiffness, $k_f = 0$. Solid lines are for the case of small folding stiffness, $k_f = 0.001$. There are three trivial zero modes (uniform translations in three directions) at the origin G of the Brillouin zone. A nonzero folding stiffness does not significantly influence the dispersion relations. (b) Dispersion relations of a topological sheet in the eggbox family. There are also three trivial zero modes at G, but two nontrivial topological zero modes appear between point M and Y (as they do for any path that intersects the red lines of isometries shown in the inset) in the absence of folding stiffness, as predicted by our analytical theory. In the absence of folding stiffness, the frequencies of the two acoustic modes scale linearly from the zero modes and verify the scaling law in Eq. (29). Increasing the folding stiffness lifts the frequencies of the two zero modes up by $O(k_f^{1/2})$.

For finite-size sheets, the wave vectors allowed by the periodic boundary conditions consist of two-dimensional grid points in reciprocal space, none of which, in general, lie precisely on the lines of soft modes. However, for modes that are *close* to this line of soft modes, there are two small quantities: the low bending modulus k_f and the small distance in reciprocal space, which we may denote by $\delta\mathbf{q}$. The eigenvalues of the rigidity matrix thus should be on the order of $|\delta\mathbf{q}|$. It follows that, for the spectral decomposition of $\mathbf{R}^T(-\mathbf{q})\mathbf{R}(\mathbf{q})$ given by $(\lambda_{\mathbf{q},i}, \mathbf{v}_{\mathbf{q},i})$, the lowest two eigenvalues $\lambda_{\mathbf{q},i}$ with $i = 1, 2$ should scale as $|\delta\mathbf{q}|^2$.

We denote by $\mathbf{u}_{\mathbf{q},i} \equiv \mathbf{v}_{\mathbf{q},i}^\dagger \mathbf{u_q}$, $\mathbf{f}_{\mathbf{q},i} \equiv \mathbf{v}_{\mathbf{q},i}^\dagger \mathbf{f}(\mathbf{q})$ the projections of $\mathbf{u_q}$ and $\mathbf{f}(\mathbf{q})$ into the direction of $\mathbf{v}_{\mathbf{q},i}$. Then, we can use Cramer's rule [53] to prove that the projection onto the first two eigenvectors dominates, so the following scaling law exists for $i = 1, 2$,

$$u_{\mathbf{q},i} \approx \frac{f_{\mathbf{q},i}}{O(1)(k_f/A) + O(1)k_s|\delta\mathbf{q}|^2}. \tag{30}$$

Thus, modes close to these topological modes are excited to a great degree, owing to the low energetic cost. The explicit derivation of the scaling law in Eq. (30) is shown in the Supplemental Material [42].

The physical interpretation of this result is that, for a topological sheet, the response $\mathbf{u_q}$ is significantly higher

near soft modes and consists mostly of the two low-energy modes $\mathbf{u}_{\mathbf{q},1}$ and $\mathbf{u}_{\mathbf{q},2}$.

It follows that the energy $E(\mathbf{q})$ stored in a wave vector close to soft modes $\mathbf{u}_{\mathbf{q}}$ is given by

$$E(\mathbf{q}) = \frac{1}{2}\mathbf{u}_{\mathbf{q}}^{\dagger}\mathbf{f}(\mathbf{q}) \approx \sum_{i=1,2} \frac{f_{\mathbf{q},i}^2}{O(1)(k_f/A) + O(1)k_s|\delta\mathbf{q}|^2}. \quad (31)$$

Consequently, the total energy of the system has contributions mainly from modes near lines of soft modes. Intuitively, this means that, since face folding costs significantly less energy than bar stretching, those modes near soft modes that do not change the lengths of any bars are energetically favored and activated to a greater degree in topological origami sheets. In the infinite-size limit, an analytical expression of the total energy can be deduced from Eq. (31) with some proper approximations. In the Supplemental Material [42], we show the total energy E_{tot} obeys the following power law:

$$E_{\text{tot}} = \int_{\text{BZ}} E(\mathbf{q}) d^2\mathbf{q} \sim \frac{|\mathbf{f}|^2}{\sqrt{k_s k_f/A}}. \quad (32)$$

The effective stiffness of the sheet, defined as $k_{\text{eff}} = |\mathbf{f}|^2/2E_{\text{tot}}$, consequently scales as $\sqrt{k_s k_f/A}$. With fixed k_s, A, for the conventional lattice, because of the absence of soft modes, its stiffness is independent of k_f and scales as k_s instead. Similar scaling laws of elastic moduli appear in other isostatic lattices [54,55].

We also have a variant of the power law derived above for the special case of a vanishing Poisson's ratio, i.e., when the topological transition occurs. At $\nu = 0$, the lines of soft modes merge into a single vertical line $q_1 = 0$ as shown in Fig. 2, and the lowest eigenvalue $\lambda_{\mathbf{q},1}$ is no longer proportional to $|\delta\mathbf{q}|^2$ but scales like $|\delta\mathbf{q}|^4$ instead. Correspondingly, Eq. (31) becomes

$$E(\mathbf{q}) \approx \sum_{i=1,2} \frac{f_{\mathbf{q},i}^2}{O(1)(k_f/A) + O(1)k_s|\delta\mathbf{q}|^4}, \quad (33)$$

and the effective stiffness now scales like $k_s^{1/4}k_f^{3/4}$. Though we make a strong assumption of working in the infinite-size limit, when deriving these power laws analytically, we find that they obey simulations of small, finite-size systems, as shown in Fig. 3.

At low folding stiffness $k_f/A \ll k_s$, because of the power law in Eq. (32), a topological sheet (as well as a transitional one) exhibits far less effective stiffness than a conventional one. Besides, since lines of soft modes emerge vertically at topological transitions, the sheet at the transition is more responsive to loads applied in the ℓ_2 lattice direction. Generalizing this observation implies that, by calculating the direction of lines of soft modes, which depends solely on the lattice Poisson's ratio ν, we can qualitatively predict an origami sheet's mechanical response with respect to different external loads without explicit experimental or numeric simulations.

Another consequence of having dominant response at finite wavelength is that the response pattern is extremely jagged for topological lattices. Analogous to the diatomic vibration case where optical phonons are associated with antiphase oscillation for neighboring particles, the vertices in neighboring cells move in different directions in topological lattices, thus creating an extremely jagged response pattern, as opposed to smooth response in conventional lattices. We discuss the numerical verification of our claims in the next section.

IV. NUMERICAL RESULTS

A. Periodic boundary condition

We begin by performing a linear calculation with periodic boundary conditions, the most analytically and numerically tractable scenario. We numerically solve the reciprocal-space matrix equation, Eq. (28), for 50×50 systems such that cells 1 and 51 are identified in each lattice direction. As shown in Fig. 4(a), we apply a force dipole to three systems: a Miura-ori, an eggbox sheet, and a Morph pattern with zero Poisson's ratio, thus at the transition point.

In each case, the mechanical response is dominated by isometric modes that do not stretch any origami panels, marked by dashed lines in Fig. 4(b). Because the Miura is topologically trivial, its only low-energy modes lie in the long-wavelength limit, and it behaves as a continuum solid sheet, with a smooth pattern of strains shown in Fig. 4(a,i). In contrast, the presence of soft modes stretching across the Brillouin zone leads to a completely different response for the eggbox, with jagged strains such that neighboring unit cells might undergo opposite deformations in Fig. 4(a,iii). For the transitional crease pattern in Fig. 4(a,ii), the straight line of soft modes in reciprocal space leads to a simple, one-dimensional line of response in real space.

As shown in Fig. 4(c), the differing patterns of spatial response also have profound effects on the effective stiffness of the sheet, the amount of force that is required to achieve a given amount of displacement. In the Miura case, there is always long-wavelength stretching of panels, and consequently, there is a finite sheet stiffness proportional to the panel stretching stiffness k_s even in the absence of folding stiffness k_f. In contrast, as predicted by Eq. (32), the eggbox's lines of soft modes mean that the response will mix folding and stretching, so the sheet's stiffness scales as $k_s^{1/2}(k_f/A)^{1/2}$. The transitional crease pattern in fact depends even more strongly on folding stiffness, with sheet stiffness scaling as $k_s^{1/4}(k_f/A)^{3/4}$ as predicted by Eq. (33).

We point out that the Fig. 4(a,iii) is expected to show an "X" shape corresponding to the X shape of lines of soft

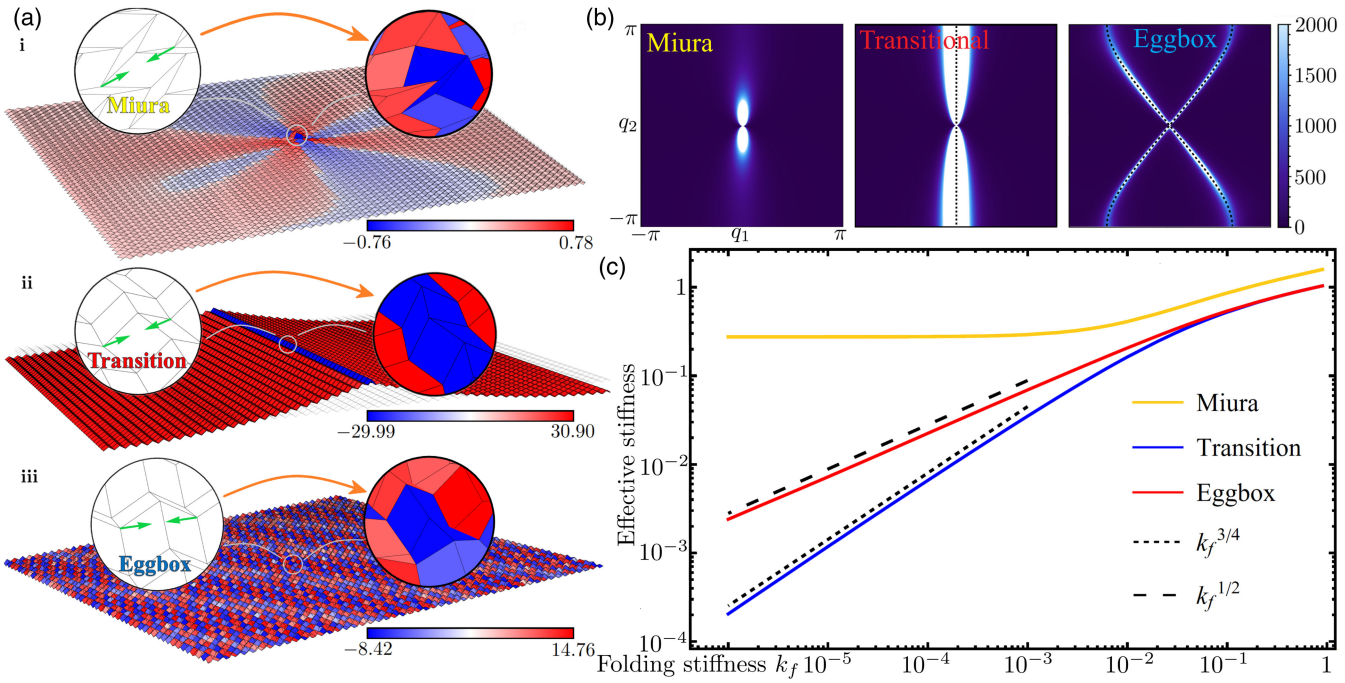


FIG. 4. (a) Loading forces (green arrows) applied in a linear, periodic model at the center of origami Morph sheets. The original positions of the edges are shown in gray, with exaggerated linearly displaced vertices. The faces are colored according to the dilational component of local strain (red when expanding and blue when compressing). The topological sheets (the eggbox and transitional one) exhibit larger deformation (in terms of root mean square of the strain) compared to the conventional Miura sheet under the same dipole loading forces. (i) Conventional Miura-type sheets undergoing a smooth, localized distortion. (ii) Sheets at the transition (zero Poisson's ratio) undergoing compression that extends to the boundaries without decay. (iii) Topological eggbox-type sheets undergoing a sharply varying set of strains that largely cancel out, leading to little net displacement. (b) Magnitude of displacement shown in reciprocal space in the Brillouin zone for the three lattices (from left to right, respectively, a Miura, a Morph at the transition point, and an eggbox sheet). For visualization convenience, all three plots are truncated so that high values in the white region are not shown explicitly, but near (dashed) lines of soft modes, the order of magnitude in the last two plots is significantly greater than that in the Miura plot (by a factor of order $1/k_f$). (c) Simulation of 50×50 finite-size systems with periodic boundary conditions. Effective stiffness of the eggbox and the transitional lattice scales, respectively, as $k_f^{1/2}$ and $k_f^{3/4}$ with fixed $k_s = 1$, verifying the power laws we derive in the main text. In addition, notice that at high folding stiffness, the system no longer prefers the folding motion, and the effective stiffness is of the same order of $k_s = 1$, reflecting a prevalence of bar stretching.

modes in reciprocal space. The two X shapes should be perpendicular to each other at the origin, which is due to the fact that, in the reciprocal space, modes with wave vectors in the directions of four branches of the X shape are highly excited and give rise to nodal lines in the perpendicular directions, which form another X shape in real space. This observation is captured by results in the open boundary condition, as shown in Fig. 5.

B. Open boundary conditions and disorder

We use MERLIN [56] to simulate origami deformation under open boundary conditions. The simulation settings and sheet parameters are specified in the Supplemental Material [42]. MERLIN is a MATLAB package designed for performing nonlinear analysis of origami, and its results agree well with real origami-based materials [11].

With open boundary conditions, the introduction of edge modes to our system invalidates the power law established in the last section. Nevertheless, bulk soft modes are well reflected in the reciprocal space, as shown in Fig. 5. However, modes at $q_1 = 0$ and $q_2 = 0$ are also possible under open boundaries, with edge modes exponentially decaying as one moves into the bulk.

This case appears in the reciprocal-space response of Fig. 5(b) as a "+" shape at the origin. Excitation at finite wavelengths still makes the response pattern drastically different for conventional and topological lattices. The Miura, a paradigm of conventional lattices, exhibits a smooth response, while the eggbox in our family of topological lattices exhibits a sharply jagged response. Finally, we mention that, even in an open-boundary system, the eggbox family tends to be less stiff than the Miura one for a generic load, while the exact stiffness depends heavily on the particular combination of the lattice Poisson's ratio and the direction of the applied load. For instance, at $\nu = 0$ where lines of soft modes appear vertically, the low-energy

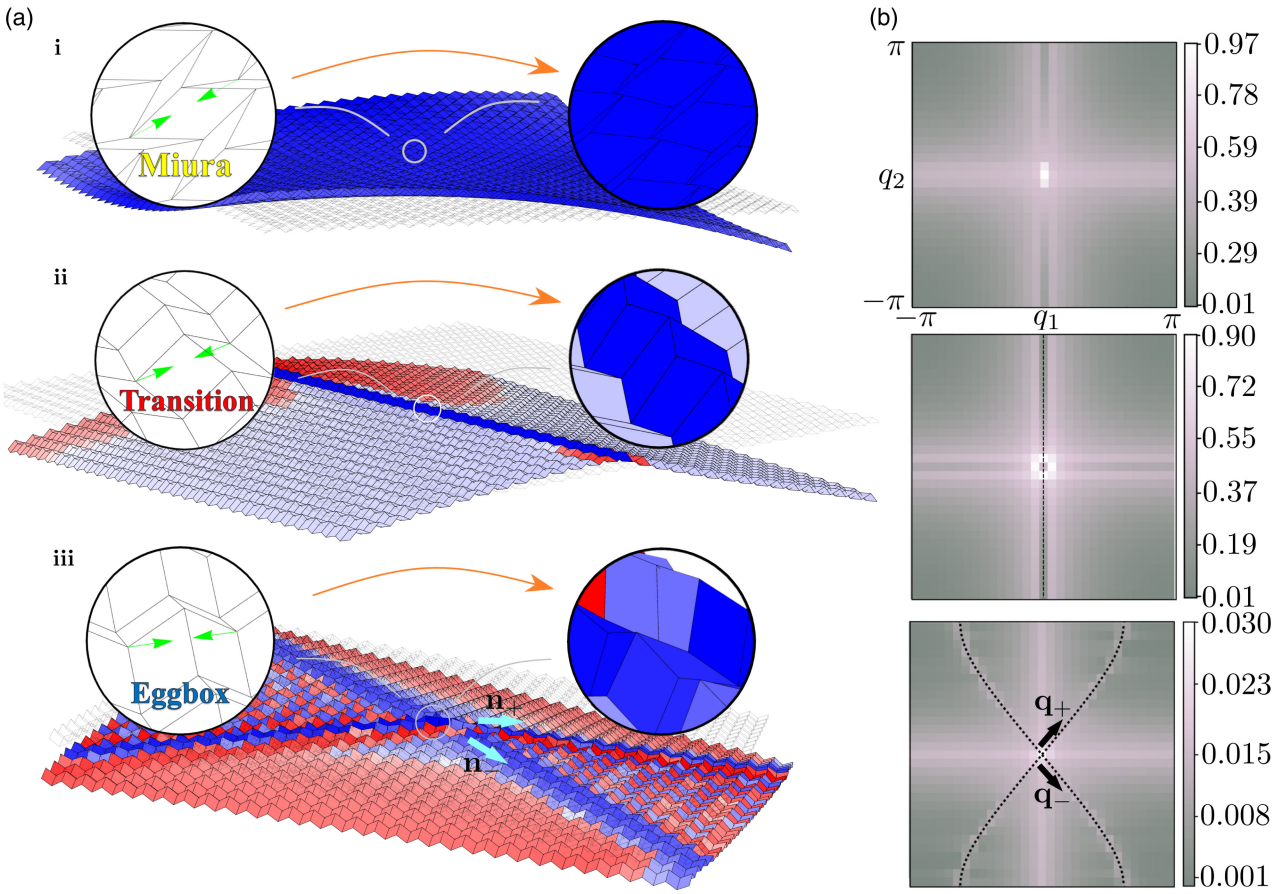


FIG. 5. Counterpart to Fig. 4 in the case of open boundary conditions. (a) Spatial embeddings of the three sheets. The external load (green arrows) is infinitesimal, and the resulting displacements are exaggerated. (i) Conventional Miura, (ii) Morph at transition $\nu = 0$, and (iii) topological eggbox, under a load at the center indicated by the pair of green arrows, with open boundary conditions. The panels are colored according to the dilation component of the in-plane strain tensor across the sheet. It is worth noting that the X-shaped blue stripe in the real space response in diagram (iii) corresponds to the X-shaped lines of soft modes in the reciprocal space by an orthogonality condition $\mathbf{k}_\pm \cdot \mathbf{n}_\mp = 0$. (b) Excited modes in reciprocal space lined up with the theoretically predicted lines of soft modes (in black). The horizontal and vertical lines across the origin $q_{1,2} = 0$ are also activated with the introduction of edge modes.

modes favored by the system are invariant in the ℓ_1 direction, i.e., $q_1 = 0$. As a consequence, it is significantly easier to pull the lattice in the ℓ_2 direction than in the ℓ_1 direction. Indeed, this idea is implied by the vanishing Poisson's ratio, which indicates that deformation in one lattice direction does not excite deformation in the other lattice direction.

In addition to open boundary conditions, we investigate how robust the results are against disorder in the geometry of the sheets. One recent experimental study of disorder [57] compared samples with disorder strength of 1%–2% and found that they had significantly different responses from a sample with negligible disorder. We perform two additional sets of MERLIN simulations, with disorder of about 1% and of about 20% (relative to the length of the lattice vectors). We randomly perturb the vertices used in Fig. 5, such that neither the rigid folding mode nor the planarity of the faces is preserved. As shown in Fig. 6(b), the response is quite similar to the no-disorder sample shown in (a), except for at the transition where the nearly one-dimensional response is distributed more widely across the sheet. Even for the highest levels of disorder shown in (c) there is a clear distinction in which the conventional sheet shows a smoother response than the nontrivial sheet, although both responses are substantially disordered. This tendency of the topological response to endure in the face of strong disorder is a hallmark of topological protection [58].

V. DISCUSSION

In this work, we show that different topological classes of parallelogram-based origami sheets can have sharply distinct mechanical response. Sheets with negative Poisson ratios have conventional, smooth, continuum fields of strain. In contrast, sheets with positive Poisson ratios have jagged and spatially irregular deformations that challenge popular existing continuum-based or homogenization-

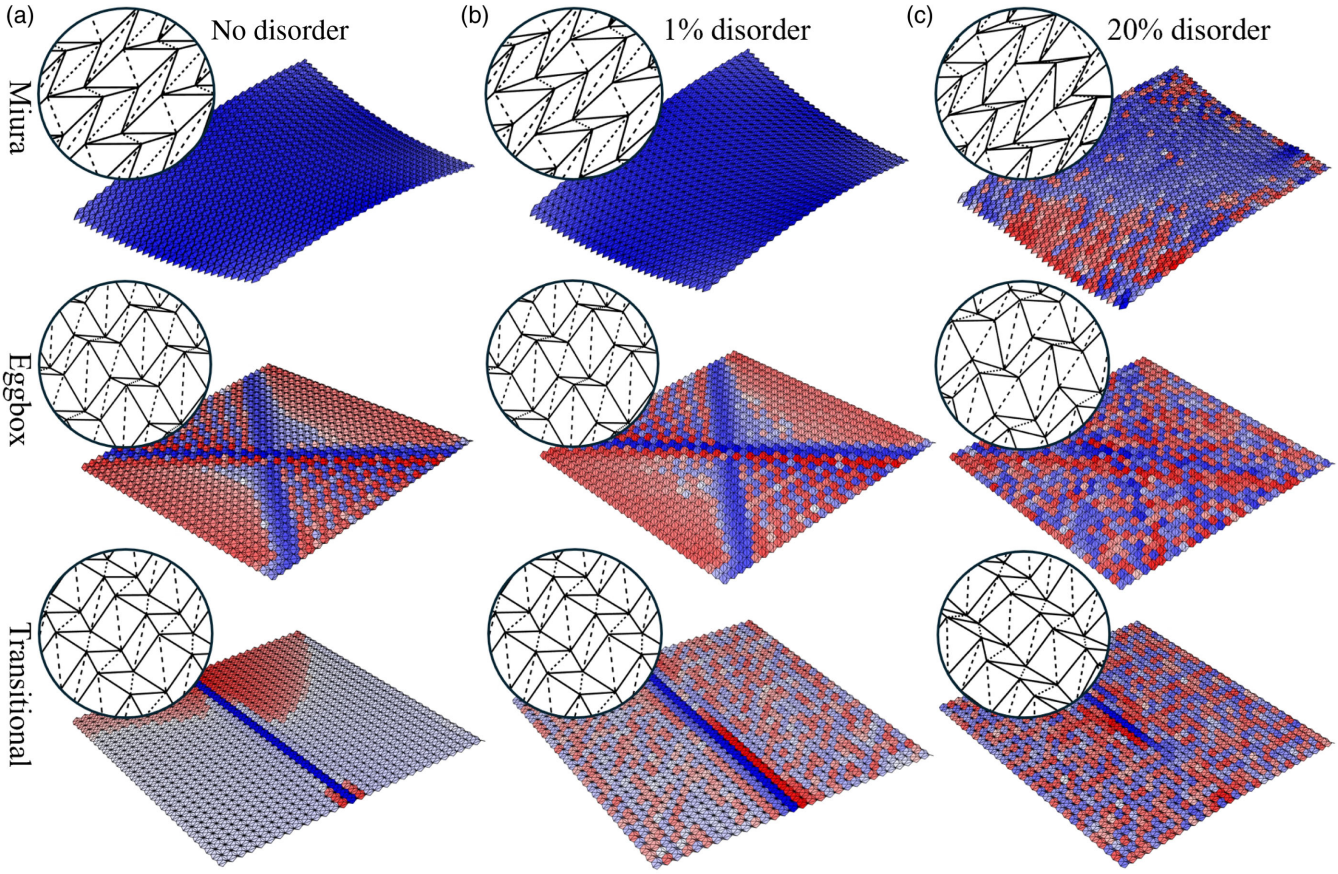


FIG. 6. Simulations under open boundary conditions when disorder is added. The three columns correspond, respectively, to zero disorder, 1%–2% disorder, and 20% disorder. The percentage is relative to the length of the lattice vectors of the sheet. Parts of the initial configurations of the sheets are shown inside the circular insets. For a 1%–2% disorder, the difference is barely noticeable. (a) Same results as in Fig. 5(a). In panel (b), when a 1%–2% disorder is present, the conventional Miura and the topological eggbox do not show any obvious discrepancy from the unperturbed situation. The Miura still has a very smooth response, while the eggbox still has a very jagged response with the same outstanding X shape at the center of the sheet. In the transitional lattice, we start to see jagged regions emerge. In panel (c), with a 20% disorder, the perturbed case starts to show a jagged response near the boundary, but overall, it is still much smoother than that of the eggbox and the transitional sheet. The X shape fades out for the perturbed eggbox, which is now qualitatively not very different from the transitional one.

based [59–62] approaches in those with positive Poisson's ratios. We show that this distinctive behavior is governed by a topological invariant, the sign of a Pfaffian, due to underlying symmetries of the system directly analogous to those present in quantum dynamics. We show that sheets for which this invariant takes on different values within the Brillouin zone, referred to here as topological lattices, possess topologically protected, doubly degenerate lines of zero modes. This theory provides a concrete way of classifying parallelogram-based origami sheets by direct calculation of this topological invariant. In contrast with the Kane-Lubensky topological polarization [23], which does not occur in origami sheets [4,27], this topological invariant strongly modifies their bulk response. While the four-parallelogram class we consider here includes popular origami sheets such as the Miura ori, the eggbox, and the Morph [30], it is unclear whether the mechanical response of other quadrilateral-based origami sheets, such as the Huffman grid and Barretto's Mars, also maps onto Hermitian quantum dynamics. Finally, using the MERLIN simulation, we extend our results to systems with open boundary conditions.

Our results provide a topological perspective of controlling origami-inspired mechanical structures, with clearly testable experimental signatures. Our approach extends to more general systems other than the four-parallelogram one discussed in the current work, as was recently shown for uniform deformations of trapezoid-based origami [43]. Therefore, there is much potential in designing desired mechanical properties by choosing different crease geometries or by dynamically reconfiguring a single sheet [30], causing topologically protected degenerate modes to emerge or vanish and consequently dramatically modifying its response. Recent advances have permitted the uniform

excitation of origami folding modes [11], with the potential for modified methods to achieve and characterize the topological modes identified here. The doubly degenerate and protected nature of the modes suggests a potential realization of a non-Abelian holonomic (analog) computing regime identified in purely two-dimensional mechanical systems [63]. Finally, the response of the origami systems —which are relatively easy to synthesize, characterize, and control—may shed light on the behavior of their quantum-mechanical analog systems as in Ref. [64].

ACKNOWLEDGMENTS

The authors acknowledge financial support from the Army Research Office through the MURI program (Grant No. W911NF2210219), and the Office of Naval Research through the MURI program (Grant No. N00014-20-1-2479) and through the National Science Foundation CAREER program (Grant No. 2338492).

[1] R. J. Lang, *Origami Design Secrets: Mathematical Methods for an Ancient Art* (CRC Press, Boca Raton, FL, 2012).
[2] Robert J. Lang, *A computational algorithm for origami design*, in *Proceedings of the Twelfth Annual Symposium on Computational Geometry* (ACM Press, New York, 1996), pp. 98–105.
[3] Erik D. Demaine and Joseph O'Rourke, *Geometric Folding Algorithms: Linkages, Origami, Polyhedra* (Cambridge University Press, Cambridge, England, 2007).
[4] James McInerney, Bryan Gin ge Chen, Louis Theran, Christian D. Santangelo, and D. Zeb Rocklin, *Hidden symmetries generate rigid folding mechanisms in periodic origami*, Proc. Natl. Acad. Sci. U.S.A. **117**, 30252 (2020).
[5] James McInerney, Glaucio H. Paulino, and D. Zeb Rocklin, *Discrete symmetries control geometric mechanics in parallelogram-based origami*, Proc. Natl. Acad. Sci. U.S.A. **119**, e2202777119 (2022).
[6] Anastasia Wickeler and Hani Naguib, *Novel origami-inspired metamaterials: Design, mechanical testing and finite element modelling*, Mater. Des. **186**, 108242 (2019).
[7] Cheng Lv, Deepakshyam Krishnaraju, Goran Konjevod, Hongyu Yu, and Hanqing Jiang, *Origami based mechanical metamaterials*, Sci. Rep. **4**, 5979 (2014).
[8] Mustafa Boyvat, Je-Sung Koh, and Robert J. Wood, *Addressable wireless actuation for multijoint folding robots and devices*, Sci. Rob. **2**, eaan1544 (2017).
[9] Yuchen Jin, Jing Li, Shiyang Liu, Gongqi Cao, and Jianlin Liu, *A worm-inspired robot based on origami structures driven by the magnetic field*, Bioinspiration Biomimetics **18**, 046008 (2023).
[10] Shengzhu Yi, Liu Wang, Zhipeng Chen, Jian Wang, Xingyi Song, Pengfei Liu, Yuanxi Zhang, Qingqing Luo, Lelun Peng, Zhigang Wu, Chuan Fei Guo, and Lelun Jiang, *High-throughput fabrication of soft magneto-origami machines*, Nat. Commun. **13**, 4177 (2022).
[11] Diego Misseroni, Phanisri P. Pratapa, Ke Liu, and Glaucio H. Paulino, *Experimental realization of tunable poisson's ratio in deployable origami metamaterials*, Extreme Mech. Lett. **53**, 101685 (2022).
[12] Hairui Wang, Danyang Zhao, Yifei Jin, Minjie Wang, Tanmoy Mukhopadhyay, and Zhong You, *Modulation of multi-directional auxeticity in hybrid origami metamaterials*, Appl. Mater. Today **20**, 100715 (2020).
[13] E. Hawkes, B. An, N. M. Benbernou, H. Tanaka, S. Kim, E. D. Demaine, D. Rus, and R. J. Wood, *Programmable matter by folding*, Proc. Natl. Acad. Sci. U.S.A. **107**, 12441 (2010).
[14] Chunlong Wang, Hongwei Guo, Rongqiang Liu, and Zongquan Deng, *A programmable origami-inspired space deployable structure with curved surfaces*, Engineering structures **256**, 113934 (2022).
[15] Christian D. Santangelo, *Extreme mechanics: Self-folding origami*, Annu. Rev. Condens. Matter Phys. **8**, 165 (2017).
[16] K. v. Klitzing, G. Dorda, and M. Pepper, *New method for high-accuracy determination of the fine-structure constant based on quantized Hall resistance*, Phys. Rev. Lett. **45**, 494 (1980).
[17] R. B. Laughlin, *Quantized Hall conductivity in two dimensions*, Phys. Rev. B **23**, 5632 (1981).
[18] Martin R. Zirnbauer, *Riemannian symmetric superspaces and their origin in random-matrix theory*, J. Math. Phys. (N.Y.) **37**, 4986 (1996).
[19] A. Altland and M. R. Zirnbauer, *Nonstandard symmetry classes in mesoscopic normal-superconducting hybrid structures*, Phys. Rev. B **55**, 1142 (1997).
[20] Krishanu Roychowdhury and Michael J. Lawler, *Classification of magnetic frustration and metamaterials from topology*, Phys. Rev. B **98**, 094432 (2018).
[21] Joel E. Moore, *The birth of topological insulators*, Nature (London) **464**, 194 (2010).
[22] W-P_ Su, J. R. Schrieffer, and A. J. Heeger, *Soliton excitations in polyacetylene*, Phys. Rev. B **22**, 2099 (1980).
[23] C. L. Kane and T. C. Lubensky, *Topological boundary modes in isostatic lattices*, Nat. Phys. **10**, 39 (2014).
[24] Roman Süsstrunk and Sebastian D. Huber, *Observation of phononic helical edge states in a mechanical topological insulator*, Science **349**, 47 (2015).
[25] Noah P. Mitchell, Lisa M. Nash, Daniel Hexner, Ari M. Turner, and William T. M. Irvine, *Amorphous topological insulators constructed from random point sets*, Nat. Phys. **14**, 380 (2018).
[26] P. Wang, L. Lu, and K. Bertoldi, *Topological phononic crystals with one-way elastic edge waves*, Phys. Rev. Lett. **115**, 104302 (2015).
[27] Bryan Gin-ge Chen, Bin Liu, Arthur A. Evans, Jayson Paulose, Itai Cohen, Vincenzo Vitelli, and C. D. Santangelo, *Topological mechanics of origami and kirigami*, Phys. Rev. Lett. **116**, 135501 (2016).
[28] Yasuhiro Miyazawa, Chun-Wei Chen, Rajesh Chaunsali, Timothy S. Gormley, Ge Yin, Georgios Theocharis, and Jinkyu Yang, *Topological state transfer in Kresling origami*, Commun. Mater. **3**, 62 (2022).
[29] S. Li, P. G. Kevrekidis, X. Mao, and J. Yang, *Topological pumping in origami metamaterials*, Phys. Rev. B **110**, 075123 (2024).
[30] Phanisri P. Pratapa, Ke Liu, and Glaucio H. Paulino, *Geometric mechanics of origami patterns exhibiting*

Poisson's ratio switch by breaking mountain and valley assignment, Phys. Rev. Lett. **122**, 155501 (2019).
[31] Arthur Cayley, *The Collected Mathematical Papers* (Cambridge University Press, Cambridge, England, 1894), Vol. 7.
[32] Charles L. Kane and Eugene J. Mele, *Z 2 topological order and the quantum spin Hall effect*, Phys. Rev. Lett. **95**, 146802 (2005).
[33] Suraj Shankar, Petur Bryde, and L. Mahadevan, *Geometric control of topological dynamics in a singing saw*, Proc. Natl. Acad. Sci. U.S.A. **119**, e2117241119 (2022).
[34] Koryo Miura and Robert J. Lang, *The science of Miura-Ori: A review*, Origami **4**, 87 (2009).
[35] Mark Schenk and Simon D. Guest, *Geometry of Miura-folded metamaterials*, Proc. Natl. Acad. Sci. U.S.A. **110**, 3276 (2013).
[36] Mark Schenk, Simon D. Guest *et al.*, *Origami folding: A structural engineering approach*, Origami **5**, 291 (2011).
[37] Hussein Nassar, Arthur Lebée, and Laurent Monasse, *Curvature, metric and parametrization of origami tessellations: theory and application to the eggbox pattern*, Proc. R. Soc. A **473**, 20160705 (2017).
[38] Mark Schenk, *Folded shell structures*, Ph.D. thesis, University of Cambridge, 2012.
[39] Evgueni T. Filipov, Tomohiro Tachi, and Glaucio H. Paulino, *Origami tubes assembled into stiff, yet reconfigurable structures and metamaterials*, Proc. Natl. Acad. Sci. U.S.A. **112**, 12321 (2015).
[40] Z. Y. Wei, Z. V. Guo, L. Dudte, H. Y. Liang, and L, *Mahadevan, Geometric mechanics of periodic pleated origami*, Phys. Rev. Lett. **110**, 215501 (2013).
[41] Scott Waitukaitis, Rémi Menaut, Bryan Gin-ge Chen, and Martin Van Hecke, *Origami multistability: From single vertices to metasheets*, Phys. Rev. Lett. **114**, 055503 (2015).
[42] See Supplemental Material at http://link.aps.org/supplemental/10.1103/gdb2-grvp for a detailed derivation of mathematical expressions such as the folding amplitude, the compatibility matrix, the scaling law, etc. It also contains the parameters we used in Mathematica and MATLAB simulations.
[43] James P. McInerney, Diego Misseroni, D. Zeb Rocklin, Glaucio H. Paulino, and Xiaoming Mao, *Coarse-grained fundamental forms for characterizing isometries of trapezoid-based origami metamaterials*, Nat. Commun. **16**, 1823 (2025).
[44] D. Zeb Rocklin, *Flexible Mechanical Structures and Their Topologically Protected Deformations* (Springer, Berlin, Heidelberg, 2020), pp. 1–16.
[45] David J. Griffiths and Darrell F. Schroeter, *Introduction to Quantum Mechanics* (Cambridge University Press, Cambridge, England, 2018).
[46] Tomá š Bzdušek and Manfred Sigrist, *Robust doubly charged nodal lines and nodal surfaces in centrosymmetric systems*, Phys. Rev. B **96**, 155105 (2017).
[47] Michael Peskin, *An Introduction to Quantum Field Theory* (CRC Press, Boca Raton, FL, 2018).
[48] Phanisri P. Pratapa, Phanish Suryanarayana, and Glaucio H. Paulino, *Bloch wave framework for structures with nonlocal interactions: Application to the design of origami acoustic metamaterials*, J. Mech. Phys. Solids **118**, 115 (2018).
[49] J. Clerk Maxwell F. R. S., *L. on the calculation of the equilibrium and stiffness of frames*, London, Edinburgh, Dublin Philos. Mag. J. Sci. **27**, 294 (1864).
[50] C. R. Calladine, *Buckminster Fuller's, "tensegrity" structures and Clerk Maxwell's rules for the construction of stiff frames*, Int. J. Solids Struct. **14**, 161 (1978).
[51] E. T. Filipov, K. Liu, T. Tachi, M. Schenk, and G. H. Paulino, *Bar and hinge models for scalable analysis of origami*, Int. J. Solids Struct. **124**, 26 (2017).
[52] A. A. Evans, J. L. Silverberg, and C. D. Santangelo, *Lattice mechanics of origami tessellations*, Phys. Rev. E **92**, 013205 (2015).
[53] Gabriel Cramer, *Introduction à l'analyse des lignes courbes* (Cramer, Genève, 1750).
[54] Xiaoming Mao and T. C. Lubensky, *Coherent potential approximation of random nearly isostatic kagome lattice*, Phys. Rev. E **83**, 011111 (2011).
[55] Chase P. Broedersz, Xiaoming Mao, Tom C. Lubensky, and Frederick C. MacKintosh, *Criticality and isostaticity in fibre networks*, Nat. Phys. **7**, 983 (2011).
[56] K. Liu and G. H. Paulino, *Highly efficient nonlinear structural analysis of origami assemblages using the MERLIN2 software*, Origami **7**, 1167 (2018).
[57] Gardoni Paolo Liu Ke, Novelino Larissa S., and Paulino Glaucio H, *Big influence of small random imperfections in origami-based metamaterials*, Proc. R. Soc. A **476**, 20200236 (2020).
[58] M. Zahid Hasan and Charles L. Kane, *Colloquium: Topological insulators*, Rev. Mod. Phys. **82**, 3045 (2010).
[59] Michael Czajkowski, James McInerney, Andrew M. Wu, and D. Zeb Rocklin, *Orisometry formalism reveals duality and exotic nonuniform response in origami sheets*, arXiv:2312.12432.
[60] Alon Sardas, Michael Moshe, and Cy Maor, *A continuum geometric approach for inverse design of origami structures*, J. Mech. Phys. Solids **196**, 106003 (2025).
[61] Hu Xu, Ian Tobasco, and Paul Plucinsky, *Derivation of an effective plate theory for parallelogram origami from bar and hinge elasticity*, J. Mech. Phys. Solids **192**, 105832 (2024).
[62] H Nassar, A. Lebée, and L. Monasse, *Curvature, metric and parametrization of origami tessellations: Theory and application to the eggbox pattern*, Proc. Math. Phys. Eng. Sci. **473**, 20160705 (2017).
[63] Michel Fruchart, Yujie Zhou, and Vincenzo Vitelli, *Dualities and non-Abelian mechanics*, Nature (London) **577**, 636 (2020).
[64] Krishanu Roychowdhury, D. Zeb Rocklin, and Michael J. Lawler, *Topology and geometry of spin origami*, Phys. Rev. Lett. **121**, 177201 (2018).